

# Eye Disease Detection AI Model

---



Topic: Glaucoma Eye Disease Detection AI Model

Team Name: Octas

Team Number: 41

Team members: Nemekhbayar Nomin, Battulga Bazarsad

---

## Table of Contents

<b>1. Introduction</b>	<b>2</b>
1.1 Background of the study	2
1.2 Analysis of existing problems	2
1.2.1 Variations in Dataset	2
1.2.2 Faulty results of Extraction of ROI	3
1.3.3 Resource Constraints:	3
1.3 Research objectives	4
<b>2. Research Background</b>	<b>4</b>
2.1 Background knowledge	4
2.2 Data Analysis	5
2.3 Server Configuration	7
<b>3. Content of the study</b>	<b>8</b>
3.1 Image Preprocessing	8
3.1.1 Image Enhancement	8
3.1.2 Locating Optic Disk (ROI Extraction)	9
3.1.3 Segmentation (Not Used for Further Processing)	12
3.2 Classification	12
3.2.1 Feature Extraction	12
3.2.1.a Cnn Model	13
3.2.1.b Hog	14
3.2.1.c LBP	15
3.2.1.d SIFT	15
3.2.2 Classification	16
<b>4. Result Evaluation and Analysis</b>	<b>17</b>
4.1 Experimental run	17
Activation Map Visualization and Attention Map Generation	18
Fundus:	19
Activation Map Visualization and Attention Map Generation	19
4.2 Evaluation Metrics and Comparison with the prior study	20
4.2.1 Metrics	20
4.2.2 Comparison with the prior studies	20
<b>5. Conclusion and Future Research Directions</b>	<b>21</b>
5.1 Conclusion	21
5.2 Future Work	22
<b>6. Development schedule and role division</b>	<b>22</b>
6.1 Schedule	23
6.2 Roles	23
<b>7. References</b>	<b>24</b>

---

# 1. Introduction

## 1.1 Background of the study

Glaucoma is a severe eye condition caused by elevated intraocular pressure, which can damage the optic nerves, leading to partial or complete vision loss. The World Health Organization (WHO) identifies glaucoma as one of the leading causes of blindness worldwide. As a slow-progressing disease, glaucoma is often only detectable in later stages, underscoring the need for early detection through retinal imaging. This study leverages deep learning-based feature extraction from retinal (fundus) images to detect glaucoma in its early stages. By focusing on analyzing the optic nerve head (ONH), we aim to develop an AI model that can identify glaucoma sooner, potentially improving patient outcomes and reducing vision loss.

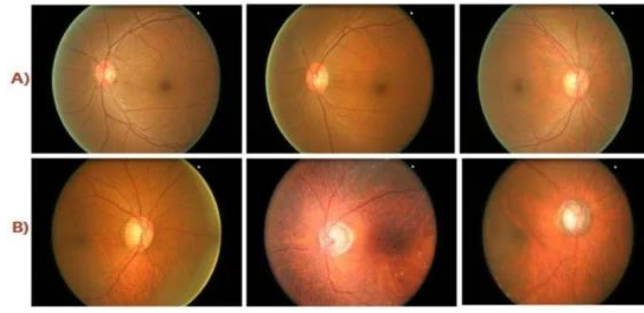


**Figure 1.** (A) Healthy Class Fundus Images; (B) Diseased Class Fundus Images.

## 1.2 Analysis of existing problems

### 1.2.1 Variations in Dataset

Our study uses three open datasets: G1020, ORIGA, and REFUGE. The G1020 dataset presents the most challenges due to its high variability and prevalence of low-quality fundus images.

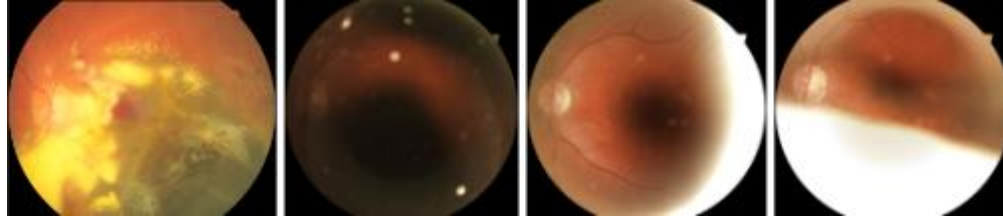


**Figure 2:** Faulty extraction examples across datasets.

### 1.2.2 Faulty results of Extraction of ROI

The ROI extraction process, initially based on a brightest spot algorithm combined with ellipse detection, struggled with inconsistent results across different datasets. Variations in image quality and noise led to inaccuracies in locating the ROI, as shown in Figure 3.

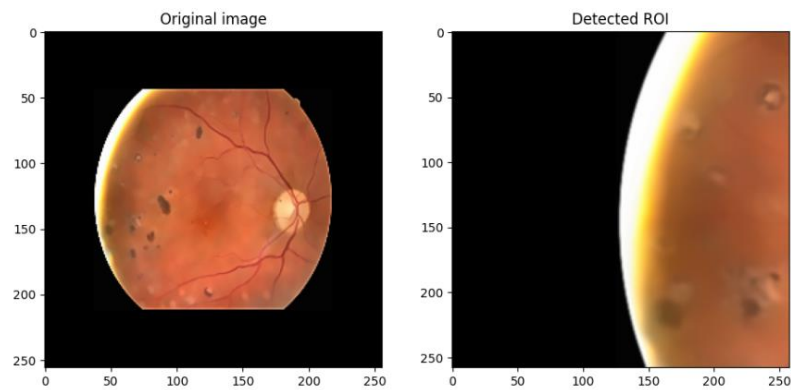


**Figure 3.** Faulty ROI extraction

### 1.3.3 Resource Constraints:

Processing and training AI models for glaucoma detection requires significant computational resources. Training models locally can be challenging without high-performance computing capabilities. Thus, developing efficient models that can operate under limited computational resources is essential.

---

## 1.3 Research objectives

This project aims to create a glaucoma detection system utilizing a combination of feature extraction techniques and machine learning classifiers to accurately diagnose glaucoma from fundus images. The objectives include:

1. **Pre-processing Fundus Images:** Apply techniques to reduce noise and enhance feature extraction accuracy.
2. **Feature Extraction:** Use CNN, HOG, LBP, and SIFT to capture a range of features pertinent to glaucoma detection.
3. **Optimal Feature Selection:** Implement MR-MR feature selection [1] to retain the most informative features.
4. **Classification Using Ensemble Methods:** Classify the extracted feature vectors using multiple classifiers, including SVM, KNN, and Random Forests.
5. **Diagnostic Output and Visualization:** Provide classification results and tools for clinicians to review feature-based diagnostics, supporting clinical decision-making.

## 2. Research Background

### 2.1 Background knowledge

Glaucoma, as a leading cause of irreversible blindness, requires early detection to mitigate significant vision loss. Fundus imaging is essential for glaucoma diagnosis as it provides detailed visuals of the optic nerve head and surrounding structures. Automated detection systems using segmentation techniques help isolate key regions of interest, such as the optic disk and optic cup, allowing a focused analysis of the optic nerve head. This approach enhances diagnostic efficiency by reducing computational overhead associated with processing irrelevant areas.

### 2.2 Data Analysis

---

The study utilizes open datasets from Kaggle, specifically:

*Glaucoma Fundus Imaging Datasets [2]* (ORIGA, REFUGE, G1020): These datasets contribute an additional 2,870 square images, uniformly sized at 512x512 pixels which is to be used in only training and testing CNN model as a feature extractor.

*SMDG-19 [3]*: The largest public fundus image repository for glaucoma AI applications, with 12,449 images uniformly sized at 512x512 pixels. Images are categorized as 0 (non-glaucoma), 1 (glaucoma), or -1 (glaucoma suspect). We excluded the -1 class to reduce ambiguity in binary classification tasks. After removing any overlapping images with ORIGA, REFUGE, and G1020, the resulting dataset contains 9,846 images (figure 4).

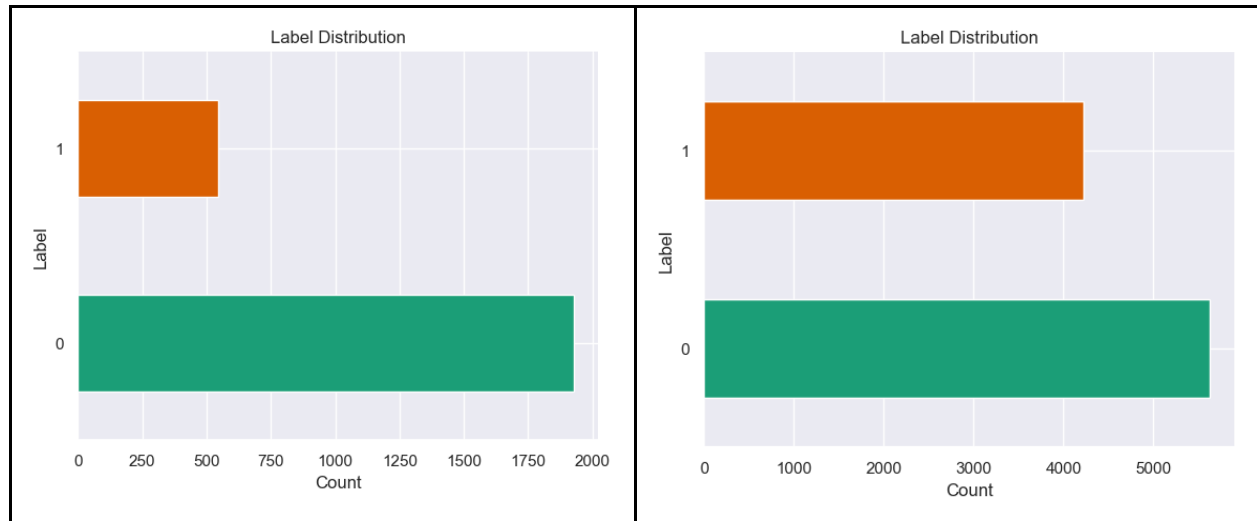


**Figure 4.** Feature Dataset Label and Classification Dataset Label

These datasets together help improve generalization across varying conditions. However, the class imbalance remains, which we address with data augmentation techniques. The augmentation was controlled through the *ImageDataGenerator* class, which included horizontal flipping and resizing, to maintain the integrity of key anatomical features. These transformations were chosen specifically to avoid excessive shifts or alterations that might obscure the optic disk or other critical areas in the fundus images.

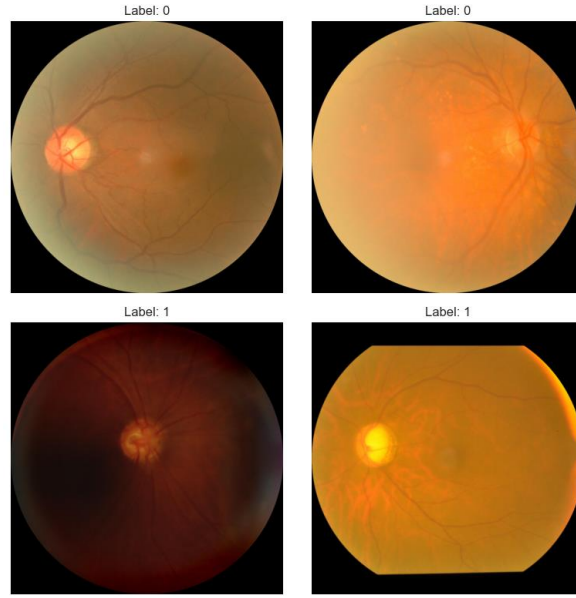


**Figure 5.** Example images from dataset

For feature extraction and classification, we divided the data to train the CNN model as a feature extractor. To further refine the data preparation, overlapping images were identified and removed, ensuring that the final dataset is free from duplicates. This approach strengthens the robustness of our model by promoting diversity in the training data.

We separated the data for training CNN model as a feature extractor and later in classification, or chose different sets. We have used another open dataset on

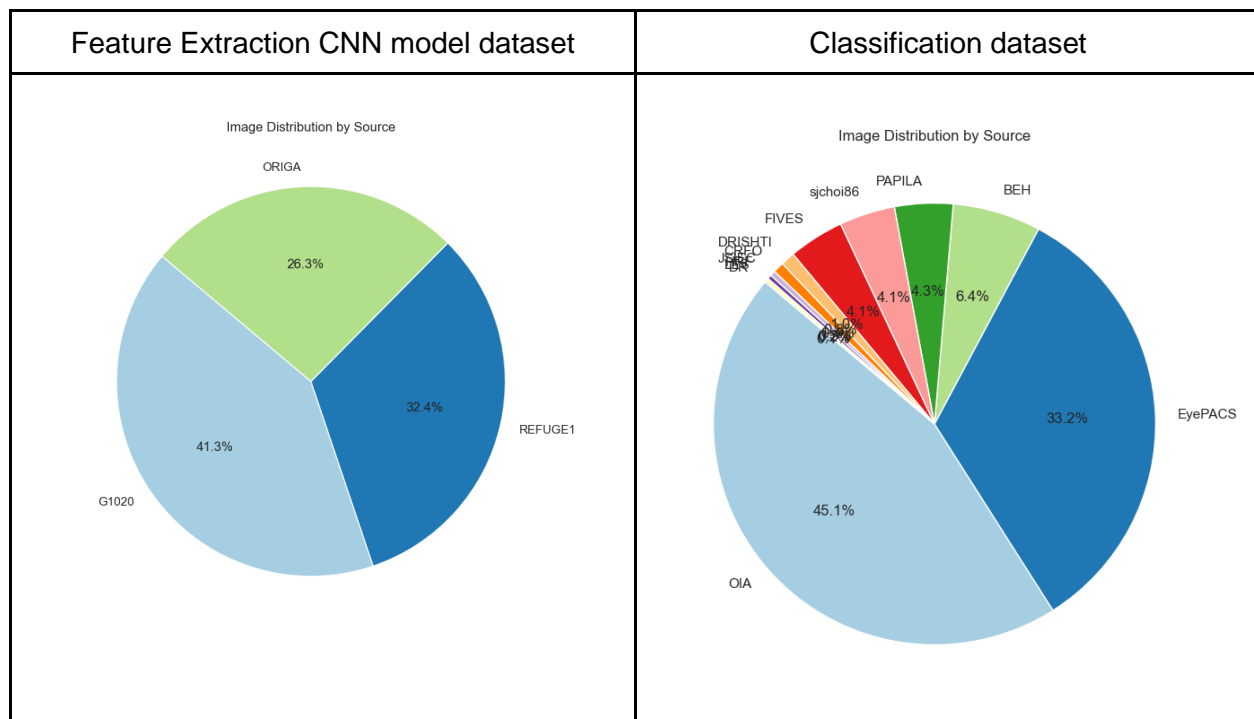


**Figure 6.** Source distributions of split datasets.

## 2.3 Server Configuration

We employed a mix of platforms:

- *Jupyter Notebook*: For local processing of large image sets, benefiting from quick data loading and initial experimentation.
- *Google Colab*: For GPU-accelerated tasks like model training and hyperparameter tuning, reducing training time and allowing integration with TensorFlow and Keras.
- *Google Drive*: For shared data storage, enabling team collaboration and ensuring access to the latest datasets and model checkpoints.



### 3. Content of the study

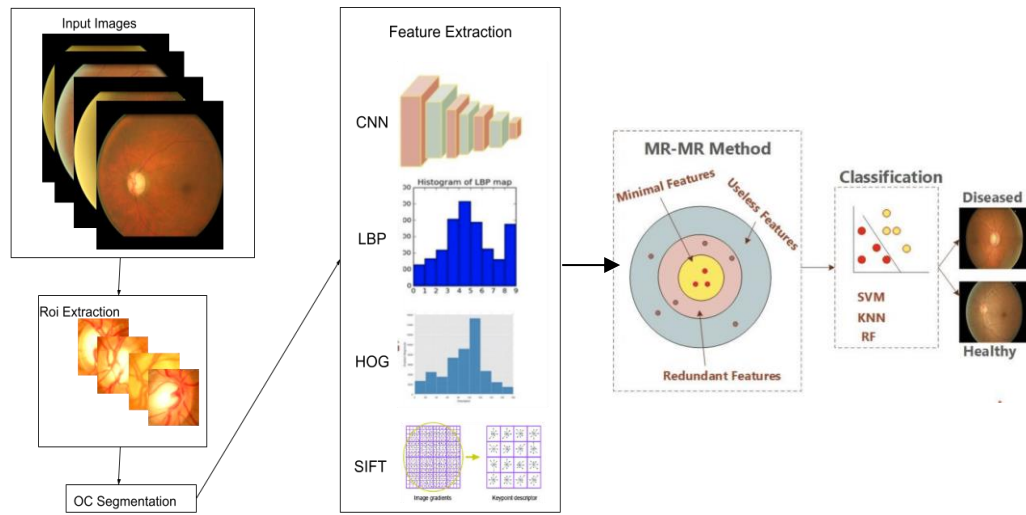


**Figure 7.** Initial Proposed base model

#### 3.1 Image Preprocessing

Effective preprocessing is crucial for glaucoma detection as it improves the input data quality, which significantly impacts model accuracy and robustness. The image preprocessing steps include enhancement, locating the optic disk, and extracting the Region of Interest (ROI).

##### 3.1.1 Image Enhancement

- Format Conversion: Images are converted to the TIFF format to preserve the image quality.
- Downscaling: The images are downscaled using a bilinear technique to reduce computational complexity and noise.
- Enhancement and Contrast: Images are enhanced and added more contrast using the CLAHE (Contrast Limited Adaptive Histogram Equalization) method for enhanced quality.

---

- Denoising: To further refine image quality, a fast Non-Local Means Denoising is applied, which effectively reduces color noise while preserving edges. This results in a cleaner image that supports reliable optic disk location and segmentation.

### 3.1.2 Locating Optic Disk (ROI Extraction)

Our proposed brightest spot algorithm alone did not show promising results, however, by combining the brightest algorithm with iteration, score function and edge detection, we achieved 99.2% accuracy in ORIGA dataset (0.8% mismatch), 98.9% accuracy in REFUGE dataset (1.1% mismatch), and 88.2% accuracy in G1020 dataset (11.8% mismatch) respectively. (figure 8).

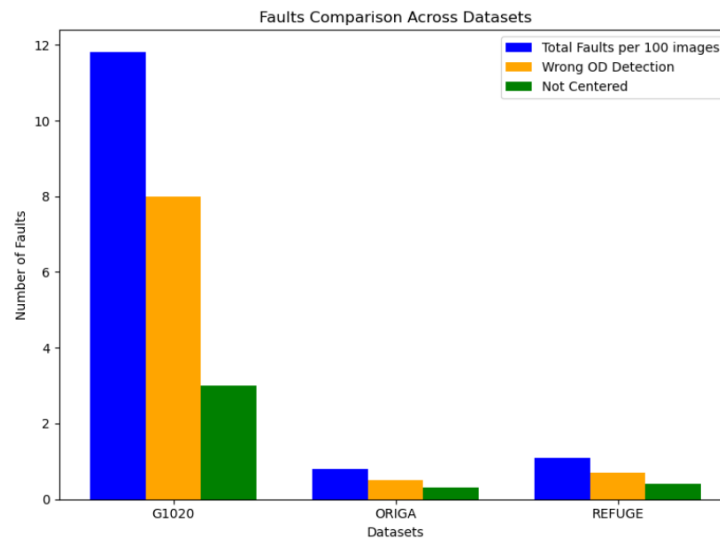


**Figure 8.** Faults comparison in G1020, ORIGA, and REFUGE datasets

**Sliding Window and Thresholding:** The algorithm iterates through the image using sliding windows of size  $(\text{height}/2) \times (\text{width}/2)$ , with steps of  $(\text{height}/4)$  and  $(\text{width}/4)$ .

Within each window, adaptive and binary thresholding methods are applied. The

---

adaptive thresholding, not explicitly mentioned earlier, is used to handle varying brightness levels within the image. (figure 9).

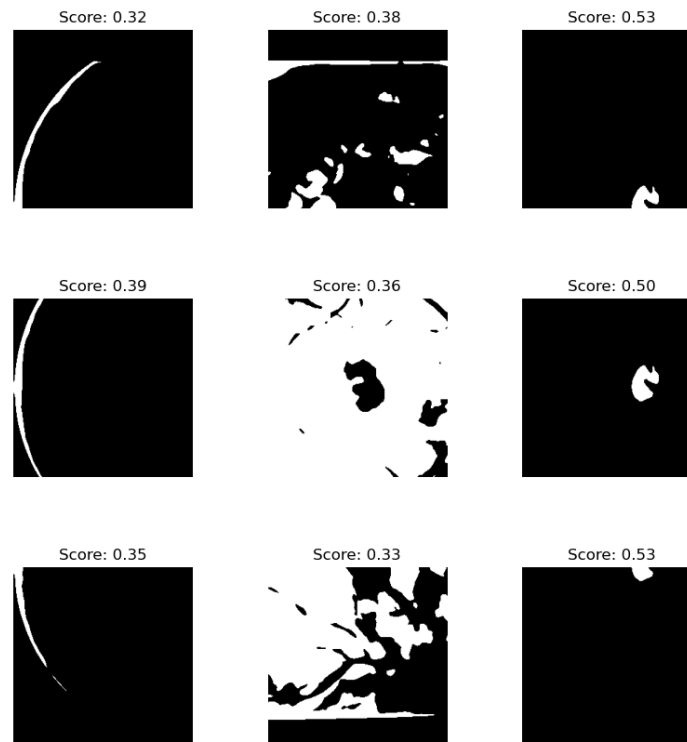


**Figure 9.** Thresholded windows

**Contour Detection and Ellipse Fitting:** After thresholding, the algorithm applies contour detection to locate the largest contour within each window. This contour is then fitted to an ellipse. For each detected ellipse, a scoring function evaluates the mean brightness, brightness standard deviation, and the aspect ratio of the ellipse. These metrics contribute to a weighted score that determines the likelihood of the region being the optic cup (figure 10).

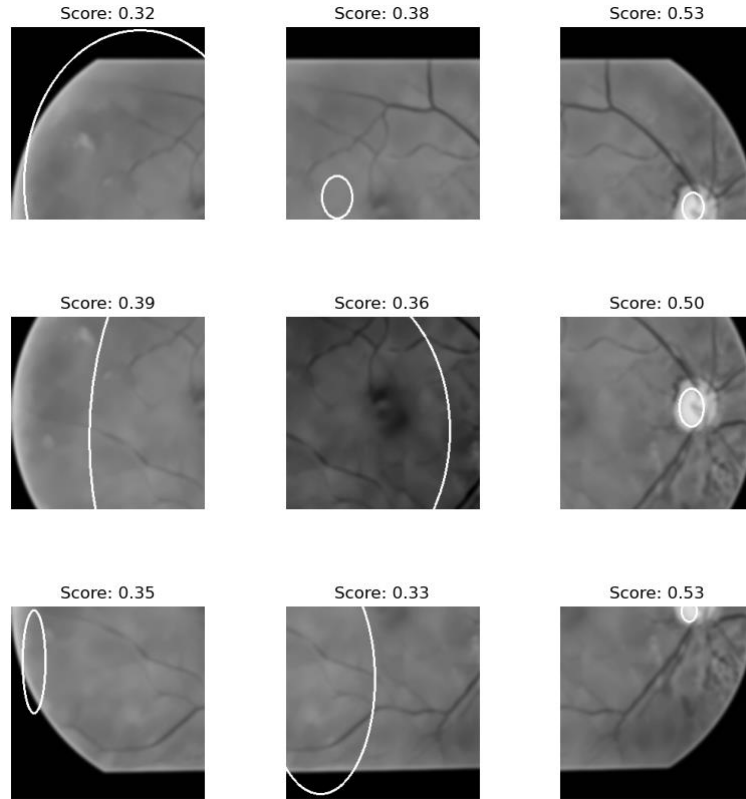


**Figure 10.** Scored ellipses in each window

**Ellipse Scoring:** The scoring function prioritizes ellipses with high mean brightness, low brightness variation, and aspect ratios close to 1, as these characteristics are common to the optic cup. The ellipse with the highest score is selected as the final ROI location (figure 10). Example output:

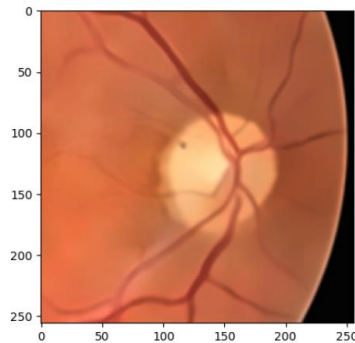


**Figure 11.** Extracted ROI

- 
- **ROI Extraction:** Once the best ellipse is identified, the algorithm crops the image around this location, adding padding based on a specified radius. This step provides a well-centered crop around the optic disk area, which will be used for further processing (figure 11).

### 3.1.3 Segmentation *(Not Used for Further Processing)*

Although segmentation using the active contour (snake) method was initially proposed as part of our approach, the evaluation results did not yield promising outcomes with segmented images. Despite early efforts to isolate the optic disk within the ROI through this method, the use of segmented images during feature extraction and classification did not lead to improvements in model performance. Consequently, we opted to use ROI-extracted images directly for further analysis, as this approach provided more consistent accuracy and better classification results. This shift in strategy is reflected in the improved performance metrics observed during the final stages of the study.

## 3.2 Classification

The input image size is fixed at (256, 256) and remains consistent throughout the classification process.

### 3.2.1 Feature Extraction

To enhance overall performance, we aim to extract both high- and low-level features from fundus images using a combination of CNN, SIFT, LBP, and HOG feature descriptors.

### 3.2.1.a Cnn Model

Model: "sequential_1"		
Layer (type)	Output Shape	Param #
conv2d_3 (Conv2D)	(None, 252, 252, 64)	4864
max_pooling2d_3 (MaxPooling 2D)	(None, 126, 126, 64)	0
conv2d_4 (Conv2D)	(None, 122, 122, 16)	25616
max_pooling2d_4 (MaxPooling 2D)	(None, 61, 61, 16)	0
conv2d_5 (Conv2D)	(None, 59, 59, 48)	6960
max_pooling2d_5 (MaxPooling 2D)	(None, 29, 29, 48)	0
activation_1 (Activation)	(None, 29, 29, 48)	0
flatten_1 (Flatten)	(None, 40368)	0
dense_1 (Dense)	(None, 2)	80738
Total params: 118,178		
Trainable params: 118,178		
Non-trainable params: 0		

**Figure 12.** Base model summary

The balanced dataset, containing ROI images from the ORIGA, REFUGE, and G1020 datasets, was used to train the CNN feature extractor model. We conducted a hyperparameter search, adjusting the number of filters in each Conv2D layer with kernel sizes between 3 and 5. The base model comprises three pairs of Conv2D and MaxPooling2D layers.

We tune and train the model with a dataset prepared for the feature extraction model and omit the last 2 output layers to use it as a feature extractor.

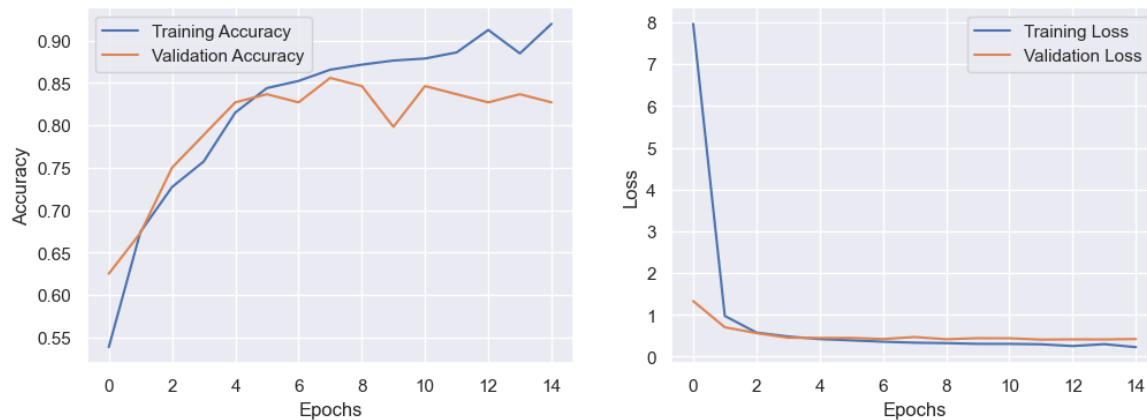


**Figure 13.** Base model and Output omitted model

While the accuracy of the model was not significantly high, it performed slightly better than other pre-trained models tested, such as VGG16 [5] , ResNet [6], and InceptionV3 [7], which yielded an average accuracy of 50%, indicating models weren't learning effectively.

Model Accuracy Comparison:

	Model	Train Accuracy	Validation Accuracy	Test Accuracy
0	Custom CNN	0.911058	0.836538	0.807692
1	VGG16	0.500000	0.500000	0.500000
2	ResNet50	0.500000	0.500000	0.500000
3	InceptionV3	0.500000	0.500000	0.500000

**Figure 14.** Comparison of models used as feature extractor

### 3.2.1.b Hog

The Histogram of Oriented Gradients (HOG) captures gradient-based texture information. Images were divided into blocks ranging from 28×28 to 6×6, each containing 2×2 cells with a stride of 4. Below are the tuning results from Bayesian Optimization [8]:

cells_per_block	orientations	pixels_per_cell	accuracy
4	6	16	0.6652
2=default	9=default	8=default	0.6595
2=default	9=default	7=custom	0.6537

The equation of pixel (x, y gradient)'s magnitude M and direction and the direction of the pixel is calculated as below:

$$M(x, y) = \sqrt{I_x^2 + I_y^2} \quad \vartheta = \tan^{-1} \frac{I_y}{I_x}$$

**Figure 15.** HOG equations

---

### 3.2.1.c LBP

Initial parameters for LBP:

LBP\_RADIUS = 2

LBP\_N\_POINTS = 16

Parameter tuning suggested `P=1` and `R=1`, but these values were deemed inadequate for capturing textural features effectively. Therefore, the original parameters were retained to capture more complex textures, resulting in a balanced representation across different spatial regions.

LBP for Texture Classification:

- Local Binary Patterns (LBP) create dual feature vectors (e.g.,  $2^K$ , where K indicates the number of adjacent pixels).
- For 16 pixels, this results in 65,536 feature vectors, with the number increasing as the size of surrounding pixels increases.

$$LBP = \sum_{i=0}^{16} k(p - c) \cdot 2^i,$$

$$k(x) = \begin{cases} 1 & \text{if } x \geq 0 \\ 0 & \text{otherwise} \end{cases}$$

**Figure 16.** The LBP's mathematical equation.

### 3.2.1.d SIFT

SIFT for Key Point and Descriptor Extraction:

The Scale-Invariant Feature Transform (SIFT) method is employed to extract key points and descriptors from the images.



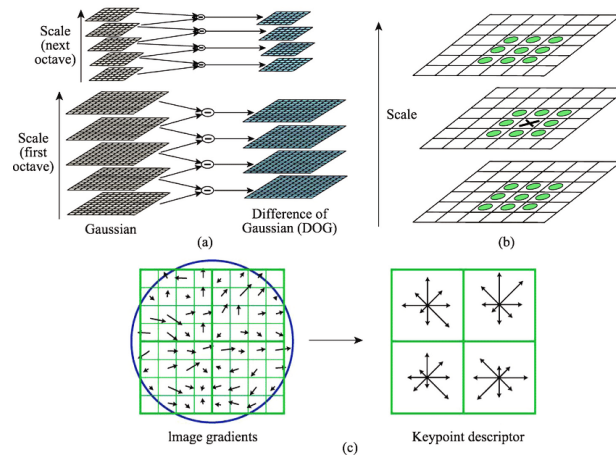


**Figure 17.** SIFT descriptor framework. (a) DoG, (b) Keypoint localization, (c) Orientation assignment and keypoint description.

### 3.2.2 Classification

Classification was conducted with the extracted features. The ensemble technique was a *soft voting classifier*. Classifiers are as follows.

- 1) *Support Vector Machine (SVM)*
- 2) *Random forest*
- 3) *KNN (K-nearest neighbor)*
- 4) *MLP(Multi Layer Perceptron)*
- 5) *XGB (Extreme Gradient Boosting) [9]*
- 6) *LR (Logical Regression)*
- 7) *GNB(Gaussian Naive Bayes) [10]*

---

## 4. Result Evaluation and Analysis

### 4.1 Experimental run

In the evaluation process, the accuracy achieved with segmented images using the active contour method did not meet our expectations, yielding a peak accuracy of only 0.750158. Initially, our method focused on isolating the optic disk within the ROI through segmentation, expecting that targeted regions would enhance feature extraction and classification accuracy. However, experimentation revealed that accuracy improved when the model was applied directly to the full fundus images, bypassing the ROI extraction process altogether.

To compare the performance across different approaches, we conducted a series of experiments using three types of inputs: segmented images, ROI-extracted images, and full fundus images. The datasets were split into 80% for training and 20% for testing. The results demonstrated that while ROI-extracted images performed better than segmented ones, full fundus images provided the highest accuracy, suggesting that preserving the complete context of the image may benefit the model's learning process.

To further understand the model's focus areas during classification, visualizations like activation maps and attention maps were generated. These visualizations indicated that the model captured more relevant features when processing full fundus images, thus supporting the decision to forego segmentation and ROI extraction for a more holistic approach.

**ROI:**

Highest Accuracy - 82.22%: SVM:  
{HOG+LBP+CNN+SIFT}

	Classifier	Features	Accuracy	Precision	Recall	F1-Score	Computation Time (s)
0	SVM	HOG+LBP+CNN+SIFT	0.822264	0.794686	0.855657	0.824045	19.596471
1	SVM	HOG	0.814674	0.804348	0.817945	0.811090	24.888311
2	SVM	HOG+CNN	0.814674	0.787440	0.847854	0.816531	19.835654
3	SVM	HOG+SIFT	0.814674	0.807494	0.812744	0.810110	24.360793
4	SVM	LBP+CNN+SIFT	0.813409	0.783493	0.851756	0.816199	19.946917
5	SVM	HOG+CNN+SIFT	0.812144	0.787805	0.840052	0.813090	19.260236
6	MLP	HOG+CNN+SIFT	0.811512	0.798479	0.819246	0.808729	7.358862
7	SVM	LBP+CNN	0.810247	0.781513	0.846554	0.812734	19.879919
8	MLP	HOG+LBP+CNN	0.810247	0.800256	0.812744	0.806452	6.533634
9	MLP	HOG+CNN	0.810247	0.792759	0.825748	0.808917	7.295884

**Figure 18.** Highest 10 accuracy table for ROI images

## Activation Map Visualization and Attention Map Generation

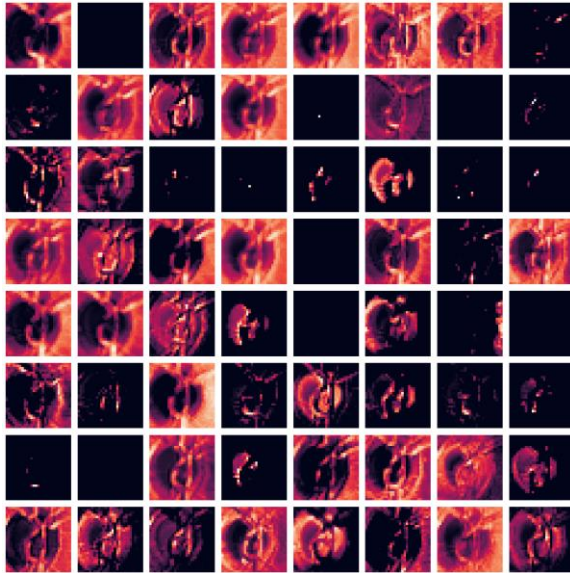


**Figure 19.** CNN Feature Extractor Attention Map on ROI Image

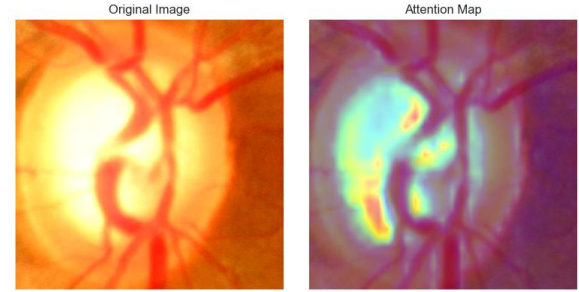


**Figure 20.** CNN Feature Extractor Heatmap on ROI Image



**Figure 21.** CNN Feature Extractor Prediction

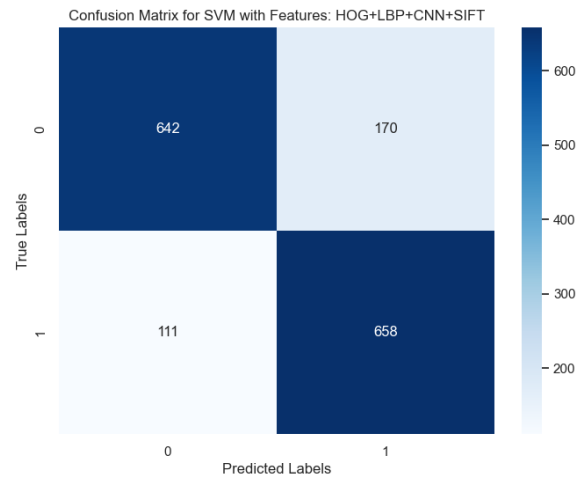


**Figure 22.** Classification Confusion matrix on ROI dataset

## Fundus:

Highest Accuracy - 84.41%: SVM: {HOG}

	Classifier	Features	Accuracy	Precision	Recall	F1-Score	Computation Time (s)
0	SVM	HOG	0.844162	0.846050	0.844162	0.842500	35.707319
1	SVM	HOG+SIFT	0.839594	0.841649	0.839594	0.837777	31.693702
2	SVM	HOG+CNN	0.839594	0.842031	0.839594	0.837647	28.536010
3	SVM	HOG+CNN+SIFT	0.839086	0.841187	0.839086	0.837242	30.699142
4	SVM	HOG+LBP+CNN	0.836041	0.839425	0.836041	0.833703	26.305526
5	SVM	HOG+LBP+CNN+SIFT	0.834518	0.836919	0.834518	0.832464	26.171071
6	MLP	HOG+LBP+CNN+SIFT	0.831980	0.831639	0.831980	0.831713	7.506870
7	MLP	HOG+LBP	0.831980	0.831680	0.831980	0.831767	7.237994
8	SVM	HOG+LBP	0.831472	0.834602	0.831472	0.829094	25.692509
9	SVM	HOG+LBP+SIFT	0.829949	0.833244	0.829949	0.827475	26.629753

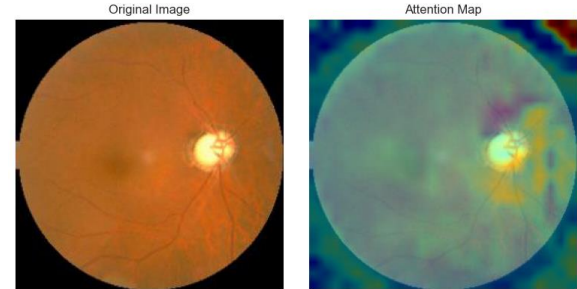


Figure 25. CNN Feature Extractor Heatmap on Fundus Image

Figure 23. Highest 10 accuracy table for fundus images

## Activation Map Visualization and Attention Map Generation

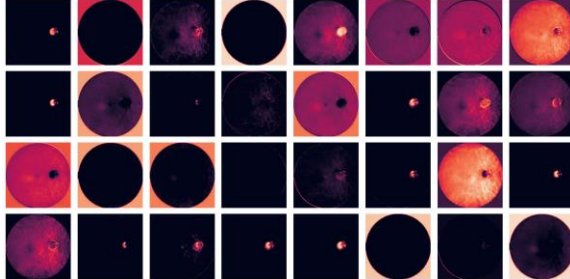


Figure 24. CNN Feature Extractor Attention Map on Fundus Image

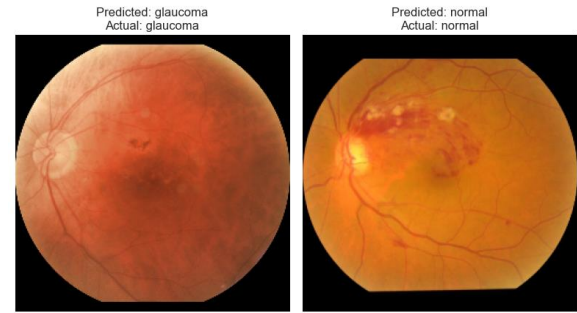


Figure 22. CNN Feature Extractor Prediction

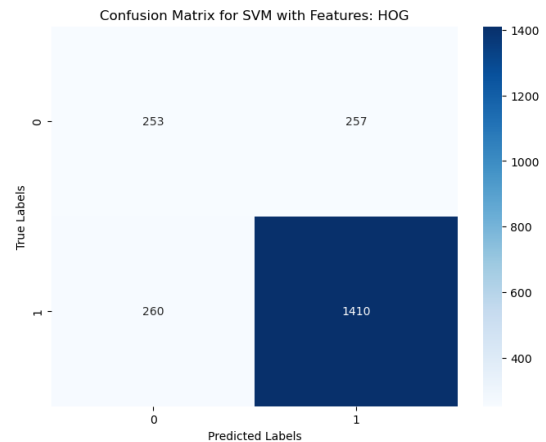


Figure 23. Classification Confusion matrix on Fundus dataset

---

## 4.2 Evaluation Metrics and Comparison with the prior study

### 4.2.1 Metrics

Various metrics have been used for the performance evaluation of the proposed model which can be shown in the confusion matrix.

*Accuracy:* Accuracy is calculated to examine the performance of the proposed system over the specific data. The equation of accuracy is shown below.

$$Accuracy = (TP + TN) / (TP + TN + FP + FN) ,$$

where true positive ( $TP$ ) denotes the total images that were classified correctly as non-healthy, whereas false positive ( $FP$ ) represents the images that were incorrectly classified as positive class such as diseased. The false negative ( $FN$ ) represents the percentage of images that our proposed method was not able to detect as non-healthy. Moreover, true negative ( $TN$ ) represents the images that are healthy and classified as healthy by our proposed system.

*Recall:* Recall  $R$  refers to the percentage of the images that were diseased and recalled by the system.

$$R = TP / (TP + FN) * 100,$$

*Precision:* Precision  $P$  refers to the ratio of the frames that are correctly classified through the proposed method. The equation of precision is given below:

$$P = TP / (TP + FP) * 100,$$

*F1 Score:* It is also known as the F Score denoted by  $F$ . The equation is given below:

$$F = 2.(P * R) / (P + R),$$

### 4.2.2 Comparison with the prior studies

In comparison to our model's results, the study by Mahum et al. (2022) achieved notable performance using various hybrid combinations of classifiers and feature

---

extraction methods. For example, they reported that using SVM with a combination of CNN and HOG yielded an accuracy of 89.3% with an F1 score of 89.54%. Meanwhile, the combination of KNN with HOG, CNN, and LBP achieved one of their highest accuracies at 97%, with an F1 score of 96.47%.

Our model, which uses a full fundus image approach rather than focusing solely on the ROI, attained an accuracy of 84.41% on the full fundus dataset, which aligns closely with the upper range of Mahum et al.'s results. Specifically, our use of SVM with HOG, CNN, and LBP resulted in an accuracy of 82.22% on ROI-extracted images, showcasing a robust yet slightly lower performance than Mahum et al.'s top configurations. This comparison underscores the strength of our approach, particularly in maintaining accuracy across diverse datasets, despite not leveraging SURF, which was part of Mahum et al.'s highest-scoring combinations.

These comparisons demonstrate that while Mahum et al.'s model achieved higher peak metrics in some configurations, our approach offers comparable performance using simpler and potentially more computationally efficient feature extraction methods. This suggests that even without the added complexity of SURF, our model can achieve competitive results for glaucoma detection in fundus images (Mahum et al., 2022).

## **5. Conclusion and Future Research Directions**

### **5.1 Conclusion**

In this study, we explored an AI-based glaucoma detection model using fundus images, where the optic disk was segmented using an active contour method. While our approach provided valuable insights into feature extraction from ROIs, we found that the accuracy of segmentation and classification was not as high as anticipated. The active contour method, though commonly used in medical image segmentation, did not yield precise enough results for glaucoma detection in our dataset. This limitation impacted the accuracy, highlighting the need for more robust segmentation techniques that can handle variations in fundus images more effectively.

---

Furthermore, we observed that using the entire fundus image as the input dataset consistently yielded better classification accuracy than using just the ROI images. This finding suggests that other areas of the retina, outside the optic disk, may contain valuable information relevant to glaucoma detection. Consequently, focusing solely on the optic disk might have restricted the model's ability to capture these additional features, thus limiting its performance.

## **5.2 Future Work**

To enhance our model, we plan to investigate a range of feature extraction techniques and classifiers to find the most effective combinations for glaucoma detection. Experimenting with advanced deep learning methods, such as using a fully convolutional network (FCN) for segmentation, might improve the precision and accuracy of the optic disk extraction process.

We also aim to delve into why the full fundus images resulted in better classification accuracy than ROI-based images. This will involve analyzing the image data to understand which specific features contribute to this improvement. It's possible that features from the retinal area surrounding the optic disk, or even from the overall texture of the retina, hold diagnostic value that aids in distinguishing between glaucoma and healthy cases. By examining these aspects, we hope to identify a more effective approach to feature extraction that leverages the entire fundus image while minimizing computational overhead.

In the long term, the goal is to refine our model to improve segmentation and classification accuracy, thereby creating a more reliable tool for early glaucoma detection. This will not only enhance diagnostic accuracy but also contribute to better patient outcomes by facilitating earlier intervention.

## **6. Development schedule and role division**

### **6.1 Schedule**

May		Jun				Jul				Aug				Sep			
3	4	1	2	3	4	1	2	3	4	1	2	3	4	1	2	3	4
Server deployment and database setup																	
		Pre-processing, ROI detection and feature extraction															
						Implementation of Feature Selection algorithm											
										Implementing Classification algorithm							
														Model Testing and Post-processing			

## 6.2 Roles

Name	Tasks
Nomin	<ul style="list-style-type: none"> <li>- Data collection and cleaning</li> <li>- Implementation of Feature Extraction algorithm</li> <li>- Implementation of Feature Selection algorithm</li> </ul>
Bazarsad	<ul style="list-style-type: none"> <li>- Image Preprocessing</li> <li>- ROI Detection algorithm</li> <li>- OC Segmentation</li> </ul>
Common	<ul style="list-style-type: none"> <li>- Deep learning model development</li> <li>- Testing and improving</li> <li>- Presentation</li> <li>- Implementation of Classification algorithm</li> </ul>



---

## 7. References

- [1] Ding, C., and H. Peng. "Minimum redundancy feature selection from microarray gene expression data." *Journal of Bioinformatics and Computational Biology*. Vol. 3, Number 2, 2005, pp. 185–205.
- [2] *Glaucoma Fundus Imaging datasets*. (2022, June 26). Kaggle.  
<https://www.kaggle.com/datasets/arnavjain1/glaucoma-datasets>
- [3] *SMDG, a standardized Fundus Glaucoma dataset*. (2023, April 23). Kaggle.  
<https://www.kaggle.com/datasets/deathtrooper/multichannel-glaucoma-benchmark-dataset>
- [3] Modified Bag of Visual Words Model for Image Classification Article's Information Abstract - Scientific Figure on ResearchGate. ([Research Gate](#))
- [4] Duda, R. O., & Hart, P. E. (1972). Use of the Hough transformation to detect lines and curves in pictures. *Communications of the ACM*, 15(1), 11–15.
- [5] Simonyan, K., & Zisserman, A. (2014, September 4). *Very deep convolutional networks for Large-Scale image recognition*. arXiv.org. <https://arxiv.org/abs/1409.1556>
- [6] He, K., Zhang, X., Ren, S., & Sun, J. (2015, December 10). *Deep residual learning for image recognition*. arXiv.org. <https://arxiv.org/abs/1512.03385>
- [7] Rethinking the inception architecture for computer vision. (2016, June 1). IEEE Conference Publication | IEEE Xplore. <https://ieeexplore.ieee.org/document/7780677>
- [8] Frazier, P., I. (2018, July 8). *A tutorial on Bayesian optimization*. arXiv.org.  
<https://arxiv.org/abs/1807.02811>

---

[9] *XGBoost Documentation* — *xgboost 2.1.1 documentation*. (n.d.).

<https://xgboost.readthedocs.io/en/stable/>

[10] Anand, M. V., KiranBala, B., Srividhya, S. R., C, K., Younus, M., & Rahman, M. H. (2022). Gaussian naïve Bayes algorithm: a reliable technique involved in the assortment of the segregation in cancer. *Mobile Information Systems*, 2022, 1–7.

<https://doi.org/10.1155/2022/2436946>

[11] Mahum, R., Rehman, S. U., Okon, O. D., Alabrah, A., Meraj, T., & Rauf, H. T. (2022). A novel hybrid approach based on deep CNN to detect glaucoma using fundus imaging. *Electronics*, 11(1), 26. [p15]. <https://doi.org/10.3390/electronics11010026>